AIAA Journal
Vol. 45, No. 12, December 2007

New Efficient High-Resolution Method for Nonlinear Problems in Aeroacoustics

S. A. Karabasov*
Cambridge University, Cambridge, England CB3 0DY, United Kingdom
and
V. M. Goloviznin†
Moscow Institute of Nuclear Safety, 115191 Moscow, Russia

DOI: 10.2514/1.29796

This paper is devoted to a new efficient numerical method for aeroacoustic applications. The method is second-order accurate, and it has a very compact numerical stencil. It combines traditional merits of finite volume and finite difference approaches such as shock capturing and linear Fourier accuracy on coarse grids.

I. Introduction

COMPUTATIONAL aeroacoustics (CAA) is an area in which efficient numerical schemes are highly demanded for nonlinear flow computations with a wide disparity of frequencies and length scales [1]. There are many successful numerical techniques used in CAA for nonlinear problems at present, but there are only a few that are designed to emphasize more than one property of the governing equations. Traditionally, higher-order versions of the basic schemes are employed to further refine a desired property. For instance, higher-order optimized finite difference schemes [1–3] use a quasi-linear form as opposed to a conservation form of the equations to mimic the Fourier properties such as linear wave dispersion and nondissipation. On the other hand, in higher-order shock-capturing finite volume schemes [4–6] or discontinuous Galerkin-type methods [7–9], it is the conservation form that is satisfied, and high-order reconstruction and interpolation procedures are employed to improve the linear properties of the basic method.

Traditional second-order shock-capturing schemes [10] are known to be too dissipative for linear wave computations on standard numerical grids. The excessive numerical dissipation in linear flow regimes is a particular bottleneck of the total variation diminishing (TVD) schemes, which use nonlinear limiter functions to eliminate nonphysical oscillations from the solution. Though efficient for shock capturing alone, the TVD schemes use a local dissipation, which reduces the approximation to first order. In addition, many finite volume TVD methods are based on improved versions of standard finite difference schemes such as Lax–Wendroff, van Leer, or central leapfrog schemes. Such standard finite difference schemes are not very suitable for aeroacoustics because they have large dissipation and/or dispersion error for a considerable part of the spectra.

A new shock-capturing method presented in this paper is also second-order accurate and it is based on the conservation form of the governing equations. The method is, however, different from standard finite volume schemes because its basic finite difference scheme has much better linear wave properties, and nonphysical oscillations are eliminated by a nonlinear procedure without smearing the linear flowfield.

II. Basic Numerical Scheme

To illustrate ideas on a simple example, a one-dimensional scalar advection equation is considered:

$$\frac{\partial \varphi}{\partial t} + \frac{\partial \varphi}{\partial x} = 0 \tag{1}$$

on a finite difference grid that is nonuniform in space $x_{i+1} - x_i = h_{i+1/2}$ and time $t^{n+1} - t^n = \tau^{n+1/2}$.

The equation is approximated by introducing dual variables referred to the same scalar quantity φ and staggered in space. A *conservative-type* variable $\psi^n_{i+1/2}$ is defined in cell centers, and an *advection-type* variable φ^n_i is defined at cell boundaries.

The linear advection equation is then approximated by second-order finite differences:

$$\frac{\psi^{n+1}_{i+1/2} - \psi^n_{i+1/2}}{\tau^{n+1/2}} + \frac{\varphi^{n+1/2}_{i+1} - \varphi^{n+1/2}_i}{h_{i+1/2}} = 0 \tag{2}$$

where the midtime-layer values are evaluated using the trapezoid rule:

$$\varphi^{n+1/2}_{i+1} = \tfrac{1}{2}\left(\varphi^n_{i+1} + \varphi^{n+1}_{i+1}\right) \tag{3}$$

To complete the system of discretised equations, an upwind second-order extrapolation formula is used:

$$\varphi^{n+1}_{i+1} = 2\psi^{n+1/2}_{i+1/2} - \varphi^n_i \tag{4}$$

The midtime-level value of the conservative variable $\psi^{n+1/2}_{i+1/2}$ in Eq. (4) is obtained at the preceding *predictor* step:

$$\frac{\psi^{n+1/2}_{i+1/2} - \psi^n_{i+1/2}}{\frac{1}{2}\tau^{n+1/2}} + \frac{\varphi^n_{i+1} - \varphi^n_i}{h_{i+1/2}} = 0 \tag{5}$$

For the actual implementation, Eqs. (2–5) are performed in the reverse order, and Eqs. (2) and (3) are replaced by a single *corrector* step (2a):

$$\frac{\psi^{n+1}_{i+1/2} - \psi^{n+1/2}_{i+1/2}}{\frac{1}{2}\tau^{n+1/2}} + \frac{\varphi^{n+1}_{i+1} - \varphi^{n+1}_i}{h_{i+1/2}} = 0 \tag{2a}$$

This finite difference scheme [Eqs. (2–5)] is explicit and stable under the Courant–Friedrichs–Lewy (CFL) condition $0 \leq \tau/h \leq 1$. Also, due to the compact computational stencil, the scheme remains second-order accurate on arbitrary spatial and temporal grids, and it

---

Presented as Paper 2415 at the 12th AIAA/CEAS Aeroacoustics Conference, Cambridge, MA, 8–10 May 2006; received 16 January 2007; revision received 10 June 2007; accepted for publication 10 August 2007.

*Royal Society University Research Fellow, Whittle Laboratory, Department of Engineering, 1 J. J. Thompson Avenue; sak36@eng.cam.ac.uk. Member AIAA.

†Professor of Computational Mathematics, 52 B. Tulskaya Street; gol@ibrae.ac.ru.

requires only one flux residual evaluation

$$\text{re}\, s^n_{i+1/2} = \left(\varphi^n_{i+1} - \varphi^n_i\right)/h_{i+1/2}$$

per time step.

Another interesting feature of the scheme includes preserving the conservation law for the kinetic energylike quantity:

$$\frac{\partial f}{\partial t} + \frac{\partial f}{\partial x} = 0; \qquad f = \varphi^2 \tag{6}$$

The additional conservation law is a direct consequence of the original differential equation (1). Multiplying Eq. (2) by

$$\left(\psi^{n+1}_{i+1/2} + \psi^n_{i+1/2}\right)/2$$

and using Eqs. (2a), (4), and (5) to rearrange equations leads to a second-order approximation of the additional conservation law (6):

$$\frac{f^{n+1}_{i+1/2} - f^n_{i+1/2}}{\tau^{n+1/2}} + \frac{\left(\varphi^{n+1/2}_{i+1}\right)^2 - \left(\varphi^{n+1/2}_i\right)^2}{h_{i+1/2}} = 0 \tag{6a}$$

where $f^n_{i+1/2}$ is a quadratic function, which is positively defined in the CFL stability region

$$f^n_{i+1/2} = \left(\psi^n_{i+1/2}\right)^2 + \frac{1}{4}(h_{i+1/2})^2 \text{CFL}(1 - \text{CFL})\left(\frac{\varphi^n_{i+1} - \varphi^n_i}{h_{i+1/2}}\right)^2$$

and $\text{CFL} = \tau^{n+1/2}/h_{i+1/2}$.

On uniform grids, Eqs. (2–5) can be rearranged to exclude the conservative variables in favor of the nodal variable to obtain a nonstaggered scheme. The result is a three-time-level finite difference scheme:

$$\frac{1}{2}\left[\frac{\varphi^{n+1}_{i+1} - \varphi^n_{i+1}}{\tau} + \frac{\varphi^n_i - \varphi^{n-1}_i}{\tau}\right] + \frac{\varphi^n_{i+1} - \varphi^n_i}{h} = 0 \tag{7}$$

which is known as the second-order upwind leapfrog [11,12] or the compact, accurate, boundary-adjustable, high-resolution technique (CABARET) scheme [13].

In terms of the computational cost, the nonstaggered scheme (7) involves slightly less operations per time step in comparison with the staggered finite-volume-like formulation [Eqs. (2–5)], due to the computation of additional variables at the cell centers. However, already in two dimensions, as will be discussed in Sec. IV, this overhead becomes less significant because the same center-cell variable corresponds to all grid directions.

The nonstaggered form is well-suited to analyze linear wave dissipation and dispersion properties. For example, a traveling wave solution $\varphi^n_m \sim \exp[i\omega \cdot \tau \cdot n - ik \cdot h \cdot m]$ can be substituted in Eq. (7) to solve the resulting algebraic equation for the frequency $\omega = \omega(k \cdot h)$. One can then determine the dissipation $\Im m[\omega(k \cdot h) \cdot \tau] \neq 0$ and the dispersion $\omega(k \cdot h) \cdot \tau - k \cdot h \neq 0$ errors as a function of different wave and Courant numbers $k \cdot h$ and τ/h. In particular, the analysis shows that the CABARET scheme is nondissipative: $\Im m[\omega(k \cdot h) \cdot \tau] = 0$ for all wave numbers $-\pi < k \cdot h < \pi$. Furthermore, the scheme is exact at three Courant numbers: $\tau/h = 0$, 0.5, and 1.

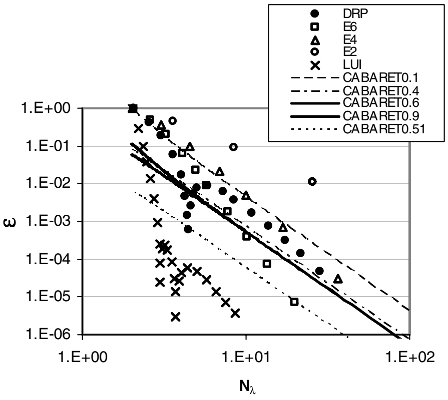

Fig. 1 Phase errors of several spatial finite difference schemes and the CABARET scheme at different CFL numbers; E2, E4, and E6 denote central differences of the second, fourth, and sixth order; DRP denotes the fourth-order dispersion relation preserving scheme of Tam and Webb [2]; LUI stands for the sixth-order pentadiagonal compact scheme of Lui and Lele [20]; and CABARET*x* stands for the CABARET scheme at a Courant number CFL = *x*.

In computational aeroacoustics, it is common to compare phase errors of different finite difference methods on a single plane, ε vs N_λ, where ε is the phase error $\varepsilon = [K(k \cdot h) - (k \cdot h)]/\pi$, and N_λ is the number of grid points per wavelengths (PPW), which is inversely proportional to the spatial wave number $N_\lambda = 2\pi/(k \cdot h)$. Measuring the decrease in numerical error with the increase of the grid resolution N_λ is useful for estimating the efficiency of the scheme [1].

The quantity $K(k \cdot h)$ represents the numerical spatial wave number obtained by substituting the spatial part of the traveling wave solution $\exp[ik \cdot h \cdot m]$ into the spatial derivative $\partial\varphi/\partial x$ discretised by finite differences. Assessing the accuracy of temporal differentiation is usually done separately, and it involves analyzing a similar quantity for the time derivative $\varepsilon_\tau = [W(\omega \cdot \tau) - (\omega \cdot \tau)]/\pi$.

For the CABARET scheme, it is the combined effect of the space and time approximation that is important, and it is the full space–time dispersion error $\varepsilon = abs[\omega(k \cdot h) \cdot \tau - (k \cdot h)]/\pi$ that characterizes the dispersion properties of the scheme.

In Fig. 1, phase errors that correspond to several spatial central finite difference schemes from [1] are shown against those of the CABARET scheme at several different Courant numbers.

It can be seen that even at the least optimal Courant number, $\text{CFL} = 0.1$, the error of CABARET scheme remains as low as that of the fourth-order central difference scheme for a wide range of PPW parameter N_λ. Furthermore, as follows from Fig. 1, in terms of computational efficiency, the CABARET scheme compares particularly well to the high-order schemes over a wide range of the phase error ε. For the spatial finite difference schemes used together with multilevel Runge–Kutta methods of the same order of accuracy as the spatial approximation, the computing cost of each scheme may be estimated as the product of the number of points in the spatial stencil at the same time level, the number of PPW $\text{N}_\lambda(\varepsilon)$ required, and the number of temporal stages used in each scheme. For accuracy $\varepsilon = 1.\text{e} - 3$, the corresponding costs are summarized in Table 1. For the CABARET scheme, the costs are calculated on the basis of a three-point stencil (i.e., two nodal values and one center-cell value, which are involved in the calculation at the same time level).

Another important property pertaining to the linear wave dispersion is the numerical group velocity $c_g = dK(k \cdot h)/d(k \cdot h)$ or $c_g = d\omega(k \cdot h)/d(k \cdot h)$ for the combined spatial and temporal error analysis. Any deviation of the numerical group speed from

Table 1 Computational costs of numerical schemes

Schemes	E4	E6	DRP	DRP (without the dip at $N_\lambda \sim 5$)	LUI	CABARETx $x = 0.1$	CABARETx $x = 0.4$, 0.6, and 0.9
Number of points per stencil	5	7	7	7	7	3	3
$N_\lambda(\varepsilon)$	20	8	5	20	3	20	9
Cost	400	336	140	420	126	60	27

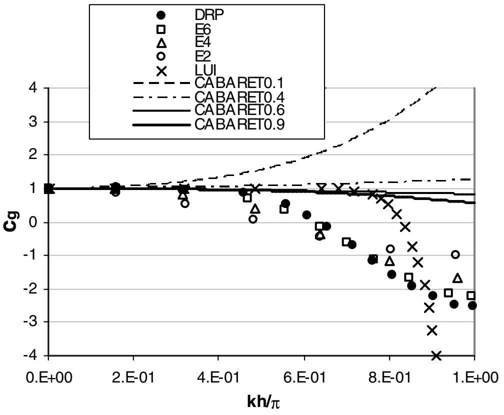

Fig. 2 Numerical group speeds of several spatial finite difference schemes and the CABARET scheme at several different CFL numbers.

unity corresponds to incorrect physical wave propagation. In particular, negative values of the numerical group speed lead to the effect of artificial wave reflection from computational grids [1].

In Fig. 2, the numerical group speeds of different spatial central finite difference schemes are shown in comparison with those of the CABARET scheme at several different Courant numbers. It can be seen that all but the highest-accuracy central schemes have regions of negative group speeds. In contrast, the negative-speed regions associated with coarse-grid reflection is not a problem for the CABARET scheme; its numerical group speed always remains in the physically correct direction. On coarse grids at the least optimal CFL number, CFL $= 0.1$, the CABARET scheme shows some abnormal linear wave dispersion effects. These errors remain relatively small in the most of the spectra, and they are comparable in magnitude to the group speed errors of the fourth-order central differences.

III. Nonlinear Procedure for Removing Nonphysical Oscillations

As with other nondissipative schemes, the CABARET scheme needs a mechanism to remove shortwave oscillations, which emerge when under-resolved gradients appear in the solution. A fundamental reason for the presence of nonphysical oscillations is a violation of the maximum principle by the numerical solution. For the scalar advection equation, the maximum principle appears as an additional constraint on the solution, which does not allow the creation of any new minima or maxima.

To reinforce this property in the numerical solution, there are nonlinear flux correction [14] methods available that use different nonlinear procedures of conservative flux modifications. Within the framework of the CABARET scheme, an appropriate nonlinear correction method is used that is based on directly satisfying the maximum principle by the solution. Specifically, in the CABARET scheme [Eqs. (2–5)], the linear extrapolation formula (4) is replaced by the following nonlinear procedure that is similar to the technique used in [15]:

$$
\begin{array}{l}
\varphi_{i+1}^{n+1} = 2\psi_{i+1/2}^{n+1/2} - \varphi_i^n \\
\max = \max\left(\varphi_i^n, \varphi_{i+1}^n, \psi_{i+1/2}^{n+1/2}\right); \quad \min = \min\left(\varphi_i^n, \varphi_{i+1}^n, \psi_{i+1/2}^{n+1/2}\right) \\
\text{if } \varphi_{i+1}^{n+1} > \max \qquad \varphi_{i+1}^{n+1} = \max \\
\text{if } \varphi_{i+1}^{n+1} < \min \qquad \varphi_{i+1}^{n+1} = \min
\end{array}
\tag{4a}
$$

The nonlinear correction procedure switches on when the solution needs to be adjusted in accordance with the local monotonicity constraint. It is noteworthy that the preceding constraint is less restrictive in comparison with standard TVD limiters, because it is not equivalent to spatial variation limiting based on local values or spatial gradients at the same time step.

The addition of the nonlinear correction does not lead to a significant increase of the cost, because logical operations are typically very fast on a computer. We estimate that the inclusion of the nonlinear correction procedure increased the overall computational cost in the tests presented for the CABARET scheme by less then 10%.

The linear Fourier analysis is difficult to apply for the CABARET scheme with the nonlinear correction and it is direct numerical computations that will be used to compare it with other schemes. The CABARET scheme with the nonlinear correction will be further referred to as the CABARET scheme.

It is first instructive to compare the CABARET scheme against other second-order schemes that also use nonlinear procedures to reinforce the maximum principle in the solution. Figure 3 shows the results of the linear advection of a rectangular pulse and a half-period sine wave for a one-stage second-order van Leer TVD scheme with MinMod and Superbee limiters and for the CABARET scheme with the nonlinear correction. These nonlinear TVD schemes are as CPU-expensive as the CABARET scheme. The computations are performed on the same periodic grid and at the same Courant number. We observed that the CABARET scheme preserves the discontinuous profile well, and it does not lead to any artificial "staircasing" of the smooth profile typical of TVD schemes at higher Courant numbers.

To compare the efficiency of the CABARET scheme against high-order optimized finite difference schemes, the linear advection test from [3] has been reproduced on a series of computational grids. In the test, the initial distribution takes the form of a sine wave modulated by a Gaussian pulse:

$$
\varphi[x_n(i), 0] = \sin\left(\frac{2\pi x_n(i)}{a \cdot h}\right) \exp\left[-\ln(2)\left(\frac{x_n(i)}{b \cdot h}\right)^2\right]
$$

$$
x_n(i) = x_n(i-1) + \frac{h}{n}
$$

In the function, two sets of parameters are considered: $(a, b) = (8, 3)$ (problem 1) and $(a, b) = (4, 9)$ (problem 2). The parameter n controls the grid resolution, and $n = 1$ corresponds to the grid used in [3]. The numerical error is defined by

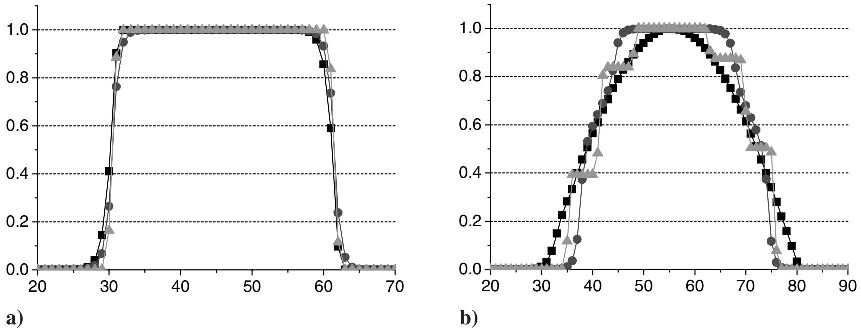

a) b)

Fig. 3 Profiles of a a) rectangle and b) half-period sine wave in 1-D linear advection tests after 250 time steps on a uniform spatial grid with $h = 1$ at CFL $= 0.45$; squares denote the solution of the CABARET scheme, and circles and triangles denote the solution of a second-order Van Leer scheme with a TVD MinMod limiter and TVD Superbee limiter, respectively.

Table 2 Errors for problem 1

	CABARET								7OS	13OS
	CFL = 0.2	0.3	0.1	0.5	0.6	0.7	0.8	0.9	0.2	0.8
$n = 1$	0.978	0.953	0.878	0.410	1.39	1.36	1.37	1.43	1.30	**0.077**
2	0.887	0.793	0.575	0.208	1.13	1.28	1.29	1.15	0.713	
4	0.576	0.416	0.217	0.104	0.420	0.564	0.563	0.421	**0.082**	
8	0.223	0.148	0.095	0.052	0.130	0.169	0.169	0.129		
16	**0.097**	**0.067**	**0.034**	**0.026**	**0.044**	**0.054**	**0.054**	**0.0448**		

Table 3 Errors for problem 2

	CABARET								7OS	13OS
	CFL = 0.2	0.3	0.4	0.5	0.6	0.7	0.8	0.9	0.2	0.8
$n = 1$	0.999	1.00	0.999	0.709	1.01	1.00	1.00	1.00	1.39	**0.077**
2	0.999	1.00	1.00	0.386	1.19	1.33	1.33	1.16	1.12	
4	1.00	0.986	0.756	0.196	1.51	1.85	1.85	1.52	0.55	
8	0.756	0.534	0.262	0.098	0.454	0.626	0.620	0.451	**0.038**	
16	0.270	0.172	0.108	0.049	0.135	0.178	0.177	0.135		
32	**0.112**	**0.079**	**0.038**	**0.024**	**0.045**	**0.056**	**0.056**	**0.045**		

$$\varepsilon = \sqrt{\frac{\sum(\varphi - \varphi_{\text{exact}})^2}{\sum \varphi_{\text{exact}}^2}}$$

In Tables 2 and 3, numerical errors are shown for the CABARET scheme for various grid refinement parameters n and Courant numbers CFL for problems 1 and 2, respectively. In the last two columns of the tables, the errors of higher-order schemes are provided. The higher-order schemes considered are the seven-point stencil dispersion-relation-preserving (DRP) scheme [2] with fourth-order-accurate Runge–Kutta time stepping (7OS) and the 13-point stencil optimized scheme used with the optimized six-stage Runge–Kutta time stepping (13OS) from the original publication [3] at recommended values of Courant number. Estimated costs per time iteration for the CABARET and the two optimized high-order schemes, 7OS and 13OS, are as follows: CABARET (48), 7OS (112), and 13OS (78) for problem 1, and CABARET (96), 7OS (224), and 13OS (78) for problem 2, which correspond to the same order of error for all schemes (bold in Tables 2 and 3). The costs are computed as a product of the grid resolution parameter, the number of points in the spatial stencil, and the number of temporal stages of each scheme.

As follows from the tables, even though the CABARET scheme is not as efficient at all tests and over all Courant numbers as the optimized spectral-like resolution scheme, it remains at a very competitive level, even with the nonlinear correction included. The nonlinear correction introduces some numerical diffusion into the pure CABARET scheme, which otherwise is most efficient for linear wave propagation, as discussed in Sec. II.

A short note on the scheme convergence may be useful. The results shown in Tables 2 and 3 are based on a relative error, as opposed to the absolute L_1 and L_2 errors, and therefore cannot be expected to have a convergence rate corresponding to the approximation order of the scheme. The same is true for convergence results of another test problem, which will be shown in Table 4, because these are based on a relative error as well. In contrast to these, as will be demonstrated later in Table 5, if the error is defined in an absolute norm in a flow computation without strong discontinuities, then the CABARET scheme shows a second-order convergence rate, in accordance with the theory.

IV. Application to Compressible Flow Equations

The extension of the CABARET scheme to the nonlinear Euler equations is obtained by introducing the dual variables of conservative-type and advection-type to describe the compressible flow both in conservation and primary form [16].

Specifically, the 2-D nonlinear Euler conservation form is given by

$$\frac{\partial \mathbf{U}}{\partial t} + \frac{\partial \mathbf{F}}{\partial x} + \frac{\partial \mathbf{G}}{\partial y} = 0; \qquad \mathbf{U}^T = (\rho, \rho u, \rho v, \rho E)$$

$$\mathbf{F}^T = (\rho u, \rho u^2 + p, \rho u v, \rho u E + u p)$$

$$\mathbf{G}^T = (\rho v, \rho u v, \rho v^2 + p, \rho v E + v p)$$

$$E = \varepsilon + (u^2 + v^2)/2 \qquad p = (\gamma - 1) \cdot \rho \cdot \varepsilon$$

and the primary form is equivalent to quasi-linear representation of the same equations:

$$\frac{\partial \mathbf{V}}{\partial t} + \mathbf{A}\frac{\partial \mathbf{V}}{\partial x} + \mathbf{B}\frac{\partial \mathbf{V}}{\partial y} = 0; \qquad \mathbf{V}^T = (\rho, u, v, p)$$

where standard notations [17] are used for the vector of conservative variables and fluxes $\mathbf{U}$, $\mathbf{F}$, and $\mathbf{G}$ and matrices of primary variables $\mathbf{A}$ and $\mathbf{B}$, where ρ is density, u and v are Cartesian velocity components, p is pressure, and ε and E are internal and total energy, respectively.

The equations in primary variables can be further rearranged into a characteristic form by using a linear change of variables to diagonalize the matrix $\mathbf{A}k_x + \mathbf{B}k_y$, where $\mathbf{k} = (k_x, k_y)$ is an arbitrary unit vector.

In multiple dimensions, the characteristic direction may be chosen to align with one of the coordinate directions x and y:

$$\begin{aligned} &\frac{\partial \mathbf{R_x}}{\partial t} + \Lambda_\mathbf{x} \cdot \frac{\partial \mathbf{R_x}}{\partial x} = \mathbf{g_x}; \qquad \delta \mathbf{R_x} = \mathbf{L_x} \cdot \delta \mathbf{V} \\ &\frac{\partial \mathbf{R_y}}{\partial t} + \Lambda_\mathbf{y} \cdot \frac{\partial \mathbf{R_y}}{\partial y} = \mathbf{g_y}; \qquad \delta \mathbf{R_y} = \mathbf{L_y} \cdot \delta \mathbf{V} \end{aligned} \tag{8}$$

where $\mathbf{L_x}$ and $\mathbf{L_y}$ are the left eigenmatrices in the x and y directions, and $\mathbf{R_x}$ and $\mathbf{R_y}$ are the vectors of Riemann quasi-invariants, which are defined in the Appendix. The source terms appearing on the right-hand side are due to the partial derivatives in the tangential direction, $\mathbf{g_x} = -\mathbf{L_x} \cdot \mathbf{B} \cdot (\partial \mathbf{V}/\partial y)$ and $\mathbf{g_y} = -\mathbf{L_y} \cdot \mathbf{A} \cdot (\partial \mathbf{V}/\partial x)$. For non-homogeneous Euler or Navier Stokes equations, the right-hand-side source terms will also include the terms arising from physical sources and/or viscous fluxes.

Similar to the scalar advection equation, the maximum principle can be introduced for the system of Euler equations in the characteristic form as an additional constraint to the governing equations. For example, in the x direction, the invariants are to be limited by

$$(\mathbf{R_x})^{\min} < \mathbf{R_x}^{t=t_0+\tau} < (\mathbf{R_x})^{\max}$$

and

$$(\mathbf{R_x})^{\min/\max} = \max/\min(\mathbf{R_x})_{t=t_0} + \int_{t_0}^{t_0+\tau} \mathbf{g_x}\, dt$$

A. Numerical Scheme

For the nonlinear Euler equations in two dimensions, the extension of the CABARET scheme is obtained similarly to Eqs. (2–5). By introducing conservative-type variables at cell centers and advection-type variables at cell faces on a rectangular Cartesian grid $\tau^n = t^{n+1} - t^n$, $x_{i+1} - x_i = \Delta x_{i+1/2}$, and $y_{j+1} - y_j = \Delta y_{j+1/2}$, conservation step (5) becomes

$$\begin{aligned} &\frac{\mathbf{U}^{n+1}_{i+1/2,j+1/2} - \mathbf{U}^{n}_{i+1/2,j+1/2}}{\tau^{n+1/2}} + \frac{\mathbf{F}^{n+1/2}_{i+1,j+1/2} - \mathbf{F}^{n+1/2}_{i,j+1/2}}{\Delta x_{i+1/2}} \\ &\quad + \frac{\mathbf{G}^{n+1/2}_{i+1/2,j+1} - \mathbf{G}^{n+1/2}_{i+1/2,j}}{\Delta y_{j+1/2}} = 0 \\ &\mathbf{F}^{n+1/2}_{i+1,j+1/2} = \frac{1}{2}(\mathbf{F}^{n+1}_{i+1,j+1/2} + \mathbf{F}^{n}_{i+1,j+1/2}) \\ &\mathbf{G}^{n+1/2}_{i+1/2,j+1} = \frac{1}{2}(\mathbf{G}^{n+1}_{i+1/2,j+1} + \mathbf{G}^{n}_{i+1/2,j+1}) \end{aligned} \tag{9}$$

where the vector of conservative variables is approximated by conservative-type variables in cell centers, and the conservative fluxes are calculated at cell faces using advection-type variables. Similar to Eq. (4), the predictor step is given by

$$\begin{aligned} &\frac{\mathbf{U}^{n+1/2}_{i+1/2,j+1/2} - \mathbf{U}^{n}_{i+1/2,j+1/2}}{\frac{1}{2}\tau^{n+1/2}} + \frac{\mathbf{F}^{n}_{i+1,j+1/2} - \mathbf{F}^{n}_{i,j+1/2}}{\Delta x_{i+1/2}} \\ &\quad + \frac{\mathbf{G}^{n}_{i+1/2,j+1} - \mathbf{G}^{n}_{i+1/2,j}}{\Delta y_{j+1/2}} = 0 \end{aligned}$$

The generalization of the extrapolation formula (3) for gas dynamics is obtained by using characteristic variables outlined as follows. Characteristic variables are associated with quasi-linear equations for which the coefficients are assumed to be locally cell-averaged. To emphasize different properties of the nonlinear flow, different representations of the locally averaged coefficients may be used. In the present paper, to obtain a self-consistent approximation for homotropic flows when the cell-averaged entropy is conserved, the left eigenmatrix is approximated by

$$\mathbf{L}_{\mathbf{x}} = \begin{pmatrix} 0 & 1 & 0 & \frac{1}{\sqrt{\gamma}}\bar{S}^{\frac{1}{2\gamma}} p^{-\frac{\gamma+1}{\gamma}} \\ 0 & 1 & 0 & -\frac{1}{\sqrt{\gamma}}\bar{S}^{\frac{1}{2\gamma}} p^{-\frac{\gamma+1}{\gamma}} \\ 0 & 0 & 1 & 0 \\ -\gamma/\rho & 0 & 0 & 1/p \end{pmatrix}$$

where

$$\bar{S} = p^{n+1/2}_{i+1/2,j+1/2} \cdot \left(\rho^{n+1/2}_{i+1/2,j+1/2}\right)^{-\gamma}$$

is a locally averaged entropy, which is defined at midtime levels and cell centers, and which is referred to the conservative-type variables. This matrix becomes an integrating factor to obtain a full differential of Riemann invariants $\mathbf{L_x} \cdot d\mathbf{V} = d\mathbf{R_x}$, where

$$\mathbf{R}^{\mathrm{T}}_{x} = [u + \bar{A}p^{\frac{\gamma-1}{2\gamma}}, u - \bar{A}p^{\frac{\gamma-1}{2\gamma}}, v, \ln(p \cdot \rho^{-\gamma})]; \qquad \bar{A} = \frac{2\sqrt{\gamma}}{\gamma - 1}\bar{S}^{\frac{1}{2\gamma}} \tag{10}$$

Having chosen a particular representation of quasi-linear matrices, the Riemann quasi-invariants are reconstructed at cell centers and faces, respectively,

$$\begin{aligned} &(\mathbf{R}_x)^n_{i+1/2,j+1/2}; \quad (\mathbf{R}_y)^n_{i+1/2,j+1/2}; \quad (\mathbf{R}_x)^{n+1/2}_{i+1/2,j+1/2} \\ &(\mathbf{R}_y)^{n+1/2}_{i+1/2,j+1/2}; \quad (\mathbf{R}_x)^n_{i+1,j+1/2}; \quad (\mathbf{R}_y)^n_{i+1/2,j+1} \end{aligned}$$

The quasi-invariants are used to update cell-face variables at the new time level. For example, in the i-grid direction, the extrapolation relations are

$$\begin{aligned} (\mathbf{R}_{q^+})^{n+1}_{i+1} &= 2(\mathbf{R}_{q^+})^{n+1/2}_{i+1/2,j+1/2} - (\mathbf{R}_{q^+})^{n+1/2}_{i} \\ (\mathbf{R}_{q^-})^{n+1}_{i} &= 2(\mathbf{R}_{q^-})^{n+1/2}_{i+1/2,j+1/2} - (\mathbf{R}_{q^-})^{n+1/2}_{i+1} \end{aligned} \tag{11}$$

where $\mathbf{R}_{q^+}$ and $\mathbf{R}_{q^-}$ are Riemann quasi-invariants going in the positive and negative direction according to the characteristic wave speeds. The wave speeds are evaluated on cell-face boundaries at the midtime-level:

$$(\mathbf{\Lambda}_{q^+})^{n+1/2}_{i+1,j+1/2}; \qquad (\mathbf{\Lambda}_{q^-})^{n+1/2}_{i,j+1/2}$$

$\mathbf{\Lambda}_{q^+} = \mathbf{\Lambda}_{q^+} + \mathbf{\Lambda}_{q^-}$; $\mathbf{\Lambda}_{q^+} > 0$; and $\mathbf{\Lambda}_{q-} < 0$, which are obtained by averaging the values at two adjacent cell centers:

$$(\mathbf{\Lambda}_{q^+})^{n+1/2}_{i+1,j+1/2} = \tfrac{1}{2}\Big[(\mathbf{\Lambda}_{q^+})^{n+1/2}_{i+3/2,j+1/2} + (\mathbf{\Lambda}_{q^+})^{n+1/2}_{i+1/2,j+1/2}\Big]$$

The characteristic extrapolation procedure results in two vectors of state obtained for each advection-type variable at the new time level for all interior cell faces.

To construct a single state vector from the available two sets of characteristic variables and eigenmatrices, the characteristic speeds inside the cell are analyzed in each coordinate direction. Inside each cell, there are four different combinations possible, which correspond to a subsonic and a supersonic fan of characteristic waves going in opposite directions. The incoming waves are assembled at each cell face to form a single state vector of variables.

In the linearization limit, the preceding procedure for solving the nonlinear Euler equations is fully nondissipative and it preserves a positively defined quadratic function similar to Eq. (6a) of the scalar equation. For small perturbations in one-dimension, the scheme becomes fully equivalent to the 1-D nonstaggered three-time-layer upwind leapfrog [12] or CABARET schemes [13].

Using characteristic variables incurs additional cost in the CABARET scheme, as it does in other second-order characteristic flux-splitting approaches, such as the van Leer or Roe schemes [17]. In addition to the conservation and interpolation steps (9) and (11), the extra cost only occurs from the recalculation of characteristic fields from the primary variables and back. But because the result for the CABARET scheme is always a multiplication product of a very sparse matrix by a vector, where the variables are defined in the same cell, it amounts to computing a simple linear combination of two variables [e.g., Eq. (10)]. Each of these computations requires a small fraction of cost in comparison with computing derivatives in conservation equation (9).

B. Nonlinear Correction Procedure

Similar to the scalar advection case, the maximum principle can be reinforced in the scheme to deal with high gradients in the solution. For nonlinear problems, this will be equivalent to emphasizing the shock-capturing property.

The nonlinear correction procedure is applied after computing the Riemann invariants on the new time level. The values obtained by upwind extrapolation (11) are adjusted if found outside the allowable monotonicity range. For example, in the x direction, this amounts to

$$\min(R_x)_{i-1/2,j-1/2} \le (R_x)^{n+1}_{i,j-1/2} \le \max(R_x)_{i-1/2,j-1/2}$$

and the tangential derivatives $(\mathbf{g}_x)^{n+1/2}_{i-1/2}$ need to be specified from the solution.

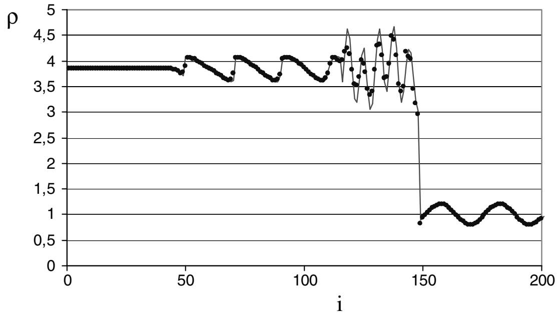

Fig. 4 Density distribution at a control time moment for a 1-D shock/density wave interaction problem, as computed on a uniform grid $N = 200$; the initial shock location corresponds to the grid cell $i = 40$.

The tangential terms can be evaluated in a computationally efficient manner, avoiding the explicit computation of tangential derivatives from the characteristic matrices. One temporal and one spatial derivative for each quasi invariant are first calculated using variables staggered in space and time in the same cell. Then these derivatives are combined into a 1-D simple wave operator of the corresponding characteristic variable, which is used to obtain the unknown tangential fields from Eq. (8). In particular, in the x-grid direction, this procedure amounts to

$$(\mathbf{g_x})^{n+1/2}_{i-1/2,j-1/2} = -\left[\frac{(\mathbf{R_x})^{n+1/2}_{i-1/2,j-1/2} - (\mathbf{R_x})^{n}_{i-1/2,j-1/2}}{\frac{1}{2}\tau^n} + (\mathbf{\Lambda_x})^{n+1/2}_{i-1/2,j-1/2} \cdot \frac{(\mathbf{R_x})^{n}_{i,j-1/2} - (\mathbf{R_x})^{n}_{i-1,j-1/2}}{\Delta x_{i-1/2}}\right] \tag{8a}$$

where

$$\min(R_x)_{i-1/2,j-1/2} = \min\left[(R_{xq})^n_{i-1,j-1/2}, (R_x)^n_{i,j-1/2}, (R_x)^{n+1/2}_{i-1/2,j-1/2}\right] + \tau^n \cdot (g_x)^{n+1/2}_{i-1/2,j-1/2}$$

$$\max(R_x)_{i-1/2,j-1/2} = \max\left[(R_x)^n_{i-1,j-1/2}, (R_x)^n_{i,j-1/2}, (R_x)^{n+1/2}_{i-1/2,j-1/2}\right] + \tau^n \cdot (g_x)^{n+1/2}_{i-1/2,j-1/2}$$

The additional CPU cost of computing simple wave operators for each characteristic variable increases the cost of the nonlinear correction procedure for the Euler equations in comparison with the 1-D scalar advection case. However, again, we note that the additional cost is not large because the cost of computing 1-D simple wave operators is low in comparison with computing the partial derivatives of the governing Euler equations.

C. Boundary Conditions

Numerical boundary conditions are specified in a characteristic fashion. On inviscid hard walls, which coincide with the boundary cell face, a zero normal velocity component is specified. The outgoing Riemann variables are computed from the interior of the boundary cell, and the incoming Riemann variable is obtained from the condition of satisfying a zero velocity normal on the wall. The pressure on the hard-wall boundary cell face is defined from the two characteristic variables similar to the internal grid points. The tangential velocity component and entropy on hard walls are found best to update by extrapolating the values from the center of the boundary cell.

The incoming Riemann variable on the cell face that coincides with an open-domain boundary is obtained by characteristic extrapolation from the freestream field. The rest of the characteristic variables are obtained from the interior.

D. Numerical Examples

1. One-Dimensional Shock/Density Wave Interaction

The benchmark problem of shock interaction with entropy waves from [4,8] challenges the capability of a numerical method to cope with linear and nonlinear flow regimes in the same calculation. In the test, the nonlinear Euler equations are solved with a moving $M_\infty = 3$ shock, which interacts with sinuous waves in density. The following initial conditions are prescribed:

$$(\rho, u, p) = (3.857143, 2.629369, 10.333333) \quad \text{for } x < -4$$

$$(\rho, u, p) = [1 + \varepsilon \sin(\lambda \cdot x), 0, 1] \quad \text{for } x \geq -4; \qquad \varepsilon = -0.2$$

$$\lambda = 5\pi; \qquad x \in [-5, 5]$$

In Fig. 4, the density distribution (solid circles) computed with the CABARET scheme on a uniform grid ($\{x_i\}$, $1 < i < N$, and $N = 200$) is shown at a control time $t = 1.8$ against the reference fine-grid solution $\{x_i\}$, $1 < i < N_{\text{ref}}$, and $N_{\text{ref}} = 9600$. At this time moment, a characteristic sawlike structure formed by the shock wave running over a perturbed density field is well-developed.

To compare against other schemes, the problem is computed on five numerical grids: $N = 200$, 400, 800, 1600, and 3200. The numerical errors and running times are summarized in Table 4. The running time corresponds to the number of time steps NT required to reach a control time moment $t = 1.8$. To be consistent with the literature, the numerical error is defined in the following two norms:

$$\varepsilon_1 = \frac{1}{N+1}\sum \frac{|\rho - \rho_{\text{exact}}|}{|\rho_{\text{exact}}|}; \qquad \varepsilon_c = Max\left(\frac{|\rho - \rho_{\text{exact}}|}{|\rho_{\text{exact}}|}\right)$$

Table 4 shows that the relative error of the CABARET scheme remains the smallest. It can also be seen that unlike the two other schemes, the CABARET scheme produces a convergence rate in the ε_1-norm that is close to 1 on all grids, including the coarser grids.

2. Two-Dimensional Advection of an Isentropic Vortex

The next example shows the capability of the scheme to accurately resolve vortical disturbances in a uniform flow. In the test [9,18], an isentropic vortex is introduced to a uniform mean flow at 45 deg to the grid lines, by perturbations in the density, velocity, and pressure. The background flow and the perturbation parameters are given, respectively, by

Table 4 Errors for the shock/density wave interaction problem

	PLIMDE[a]			WENO[b]			CABARET		
N	NT	ε_1	ε_c	NT	ε_1	ε_c	NT	ε_1	ε_c
200	250	0.0185	0.429	334	0.0214	0.902	**229**	**0.0219**	**0.1211**
400	468	0.0183	0.188	634	0.0195	0.667	**462**	**0.0100**	**0.1467**
800	903	0.0166	0.290	1235	0.0162	0.369	**927**	**0.0058**	**0.2400**
1600	1774	0.0070	0.185	2443	0.0040	0.572	**1856**	**0.0022**	**0.5338**
3200	3514	0.0024	0.230	4857	0.0013	0.399	**3716**	**0.0013**	**0.1324**

[a] PLIMDE is a second-order parabolic interpolation method.

[b] WENO is a weighted essentially nonoscillatory scheme.

Table 5 Numerical errors and costs for the 2-D vortex advection problem

N		CABARET	C4[a]	WENO[b]	ENO[c,e]	MUSCL[d,f]	WENO[e,f]
1	Error	6.9e − 4	1.1e − 3	9.3e − 4	7.8e − 4	1.2e − 3	6.1e − 4
	Cost	5	40	70	30	30	70
4	Error	1.8e − 4	**5.7e − 5**	**7.0e − 5**	**6.6e − 5**	**2.7e − 4**	**4.5e − 5**
	Cost	20	**160**	**280**	**120**	**120**	**280**
16	Error	**5.0e − 5**	3.7e − 6	2.4e − 6	7.8e − 6	5.3e − 5	2.9e − 6
	Cost	**80**	640	1120	480	480	1120

[a] C4 is a fourth-order-accurate conservative centered scheme.

[b] WENO is a standard fifth-order weighted essentially nonoscillatory scheme.

[c] ENO is a third-order essentially nonoscillatory scheme.

[d] MUSCL is a third-order van Leer variable extrapolation scheme.

[e] WENO is a modified fifth-order WENO based on the fourth-order conservative central-difference scheme.

[f] The C4 scheme is used as the basic scheme.

$$(\rho_\infty, u_\infty, v_\infty, p_\infty) = (1, 1, 1, 1)$$

and

$$\rho' = \rho_\infty\left[\left(1-\frac{(\gamma-1)\alpha^2}{8\pi^2\gamma}\exp\{1-(x-x_0)^2-(y-y_0)^2\}\right)^{1/(\gamma-1)}-1\right]$$

$$u' = -(y-y_0)\frac{\alpha}{2\pi}\exp\{0.5[1-(x-x_0)^2-(y-y_0)^2]\}$$

$$v' = (x-x_0)\frac{\alpha}{2\pi}\exp\{0.5[1-(x-x_0)^2-(y-y_0)^2]\}$$

$$p' = p_\infty\left[\left(1-\frac{(\gamma-1)\alpha^2}{8\pi^2\gamma}\exp\{1-(x-x_0)^2-(y-y_0)^2\}\right)^{\gamma/(\gamma-1)}-1\right]$$

$$\alpha = 5$$

As in [9,18], the problem is solved in a periodic domain $[0, 10] \times [0, 10]$ on a set of grids 40 by 40, 80 by 80, and 160 by 160, which correspond to grid refinement parameters $n = 1$, 4, and 16. Similar to [18], the numerical error is based on density and defined as

$$L_1 = \frac{1}{(N+1)^2}\sum_{i=0}^{N}\sum_{j=0}^{N}|\rho_{i,j} - \rho_{i,j}^{\text{exact}}|$$

In Table 5, the errors of several finite difference schemes from [18] and the CABARET scheme are shown for a control time moment $t = 2$. It can be seen that the convergence results of the CABARET scheme shown in this table are in a good agreement with the theoretically expected rate based on the order of approximation. For each scheme, the number of operations per time step (the cost) is evaluated as a product of the grid refinement parameter, the number of points in the spatial stencil, and the number of temporal stages.

Figure 5 shows instantaneous density profiles in the vortex cross section at $y = 5$ and the reference analytical solution for two later time moments, $t = 10$ and 100, on a grid of 100 by 100 cells. It can be seen that both the phase and the amplitude of the vortex are well preserved during its advection over long distances.

3. *Two-Dimensional Double Mach Reflection*

This problem is originally from [19] and has since been used in validation of high-resolution computational methods [6,8]. In a square computational domain $[0, 4] \cdot [0, 1]$, the reflective wall lies on the bottom, starting from $x = 1/6$. At the starting point of the CFD solution, the right moving $M_\infty = 10$ shock, which makes an angle of 60 deg with the x axis, crosses the bottom boundary at $x = 1/6$. The left and right states of the shock of a polytropic gas with specific heat ratio $\gamma = 1.4$ are given by, respectively,

$$(\rho, u, v, p)^{\text{right}} = (1.4, 0, 0, 1.4)$$

$$(\rho, u, v, p)^{\text{left}} = (8, 7.14471, -4.125, 116.5)$$

At the other boundaries, the flow parameters describe the exact motion of a Mach-10 shock. The benchmark problem is solved on three uniform grids of 480 by 120 cells, 960 by 240 cells, and 1920 by 480 cells. Figure 6 shows computed density fields at a control time $t = 0.2$.

It can be seen that as the grid becomes more refined, the finer flow structure with small eddies in the vicinity of the λ shock becomes

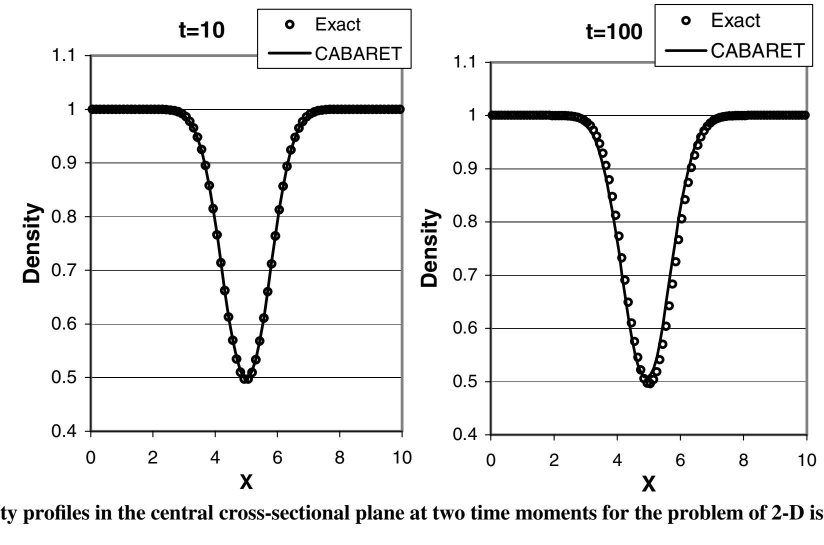

Fig. 5 Instantaneous density profiles in the central cross-sectional plane at two time moments for the problem of 2-D isentropic vortex advection in a uniform mean flow.

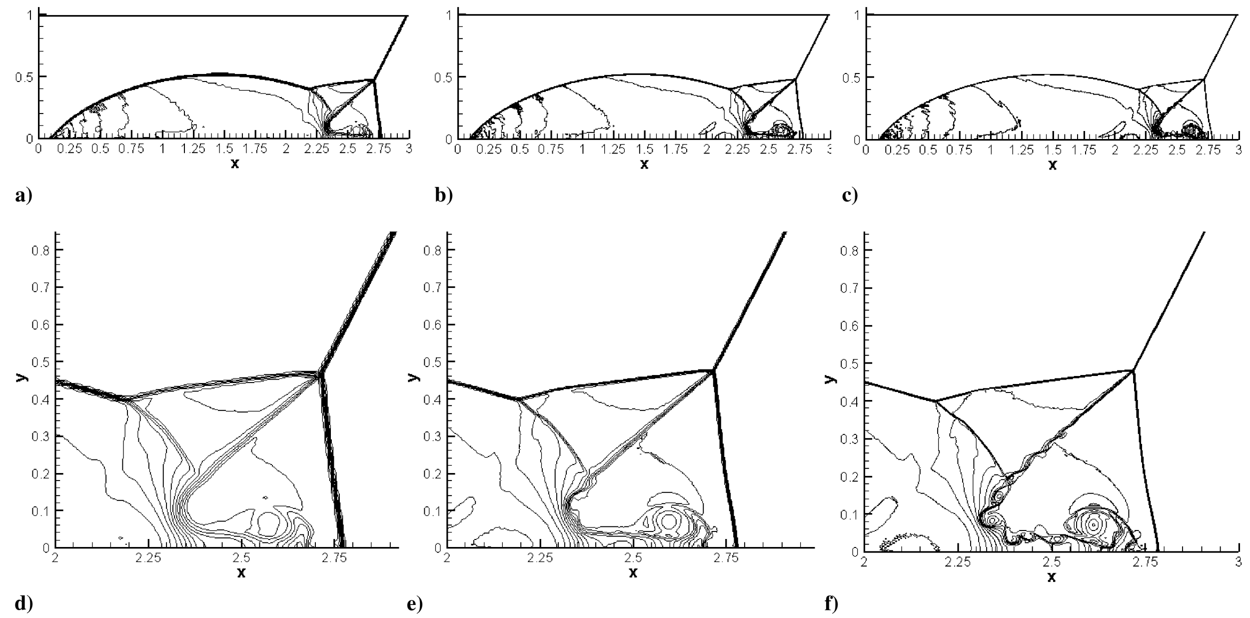

a) b) c)

d) e) f)

Fig. 6 Density fields for the double Mach reflection problem; computational grids a) 480 by 120 cells, b) 960 by 240 cells, c) 1920 by 480, and d–f) close-up views for the same grids as in Figs. 6a–6c; 30 density contours are plotted from 1 to 22.

more visible. These vortices grow with time and may be attributed to the development of the Kelvin–Helmholz instability, which occurs in inviscid flows with shear gradients. The fact that these are not suppressed by numerical viscosity indicates that the overall scheme has very low numerical dissipation. The fine flowfield structure observed is in good agreement with predictions of more CPU expense per time iteration methods, a high-order discontinuous Galerkin [8] and an arbitrary derivative (ADER) scheme [6], computed on the same grids.

4. *Two-Dimensional Shock/Vortex Interaction*

An interesting 2-D flow test from [4,18] in which complex linear and nonlinear flow structures interact is next considered.

A normal shock wave is stationary at $x = 0.5$ in a rectangular computational domain of $[0, 2] \cdot [0, 1]$, the top and bottom boundaries of which are both reflective. The left and right states of the shock in a polytropic gas with a specific ratio $\gamma = 1.4$ are given by

$$(\rho, u, v, p)^{\text{left}} = (1, 1.301538, 0, 1)$$

$$(\rho, u, v, p)^{\text{right}} = (1.169082126, 1.11329865, 0, 1.245)$$

which corresponds to the pressure ratio across the shock equal to 1.245. In the upstream region, an isentropic vortex is initiated at location (0.25,0.5) by perturbing the density, velocity, and pressure of the upstream state of the shock via the following relations:

$$\rho' = \rho^{\text{left}}\left[\left(1 - \frac{(\gamma - 1)}{4\alpha\gamma}\varepsilon^2 \exp\{2\alpha(1 - \tau^2)\}\right)^{\frac{1}{\gamma-1}} - 1\right]$$

$$u' = \varepsilon\tau \exp\{\alpha(1 - \tau^2)\} \sin\theta$$

$$v' = -\varepsilon\tau \exp\{\alpha(1 - \tau^2)\} \cos\theta$$

$$p' = \rho^{\text{right}}\left[\left(1 - \frac{(\gamma - 1)}{4\alpha\gamma}\varepsilon^2 \exp\{2\alpha(1 - \tau^2)\}\right)^{\frac{\gamma}{\gamma-1}} - 1\right]$$

$$\tau = r/r_c; \qquad r = \sqrt{(x - x_0)^2 + (y - y_0)^2}$$

$$\theta = \tan^{-1}[(y - y_0)/(x - x_0)]$$

The computation is conducted on a uniform grid of 400 by 200 cells. A weak vortex with parameters $\varepsilon = 0.3$, $r_c = 0.05$, and $\alpha = 0.204$ is considered first. The maximum pressure ratio across the weak vortex is 1.065, which is less than the shock strength.

In Fig. 7, the evolution of the pressure field is shown in several time moments. The stretching and bifurcation of the shock during the process are clearly captured and the reflection of the shock at the top boundary is well resolved. The computation results are in a good qualitative agreement with those of the high-order nonlinear filtering method of [18].

To test the robustness of the method, the same problem is calculated for a strong-vortex case, where $\varepsilon = 1.5$, $r_c = 0.05$, and $\alpha = 0.5$. The parameters correspond to a maximum pressure ratio across the vortex of 1397, which is three orders of magnitude as large as the strength of the shock. The numerical difficulty in coping with this tornado-type vortex is that the pressure in its center is so small and the velocities in the vicinity of the center are so high that negative pressure values would appear if the numerical errors were not well controlled.

In Fig. 8, the evolution of the pressure field is shown at similar time moments as in Fig. 7. In comparison with the previous case, the strong vortex leads to a completely different evolution of the flowfield. The vortex is so strong that it breaks the shock in the middle. Multiple shocks are generated and transmitted through each other; however, they get fully destroyed when they meet the vortex core at the center.

5. *Evolution of a Two-Dimensional Gaussian Pulse in an Open Domain*

Finally, to test the capability of a numerical procedure to accurately resolve and transmit acoustically small fluctuations on nonsmooth computational grids in open domains, the evolution of initial pressure disturbance in a free space is considered.

At the initial time moment, an isentropic Gaussian pressure pulse

$$p' = \varepsilon \cdot \exp\{-\beta \cdot [(x - x_0)^2 + (y - y_0)^2]\}$$

$[\beta = 0.4 \ln(2)]$ is specified in the center of a computational domain ($-3 \leq x \leq 3$ and $-3 \leq y \leq 3$) with open boundaries as a perturbation to uniform flowfields $\rho_\infty = 1$, $u_\infty = 0$, $v_\infty = 0$, and $p_\infty = 1/\gamma$, where $\varepsilon = 1.\text{e} - 5$.

In the test, the problem is computed in a half computational domain ($-3 \leq x \leq 3$ and $0 \leq y \leq 3$) with a symmetry condition at the bottom boundary, $y = 0$. A uniform Cartesian grid is used in the left part of the domain ($-1 \leq x \leq 3$ and $0 \leq y \leq 3$) of 73 by 50 cells and a stretched uniform grid, which is obtained by stretching the original grid three times in the axial direction, is used in the remaining part of the domain ($-3 \leq x < -1$ and $0 \leq y \leq 3$) of 9 by

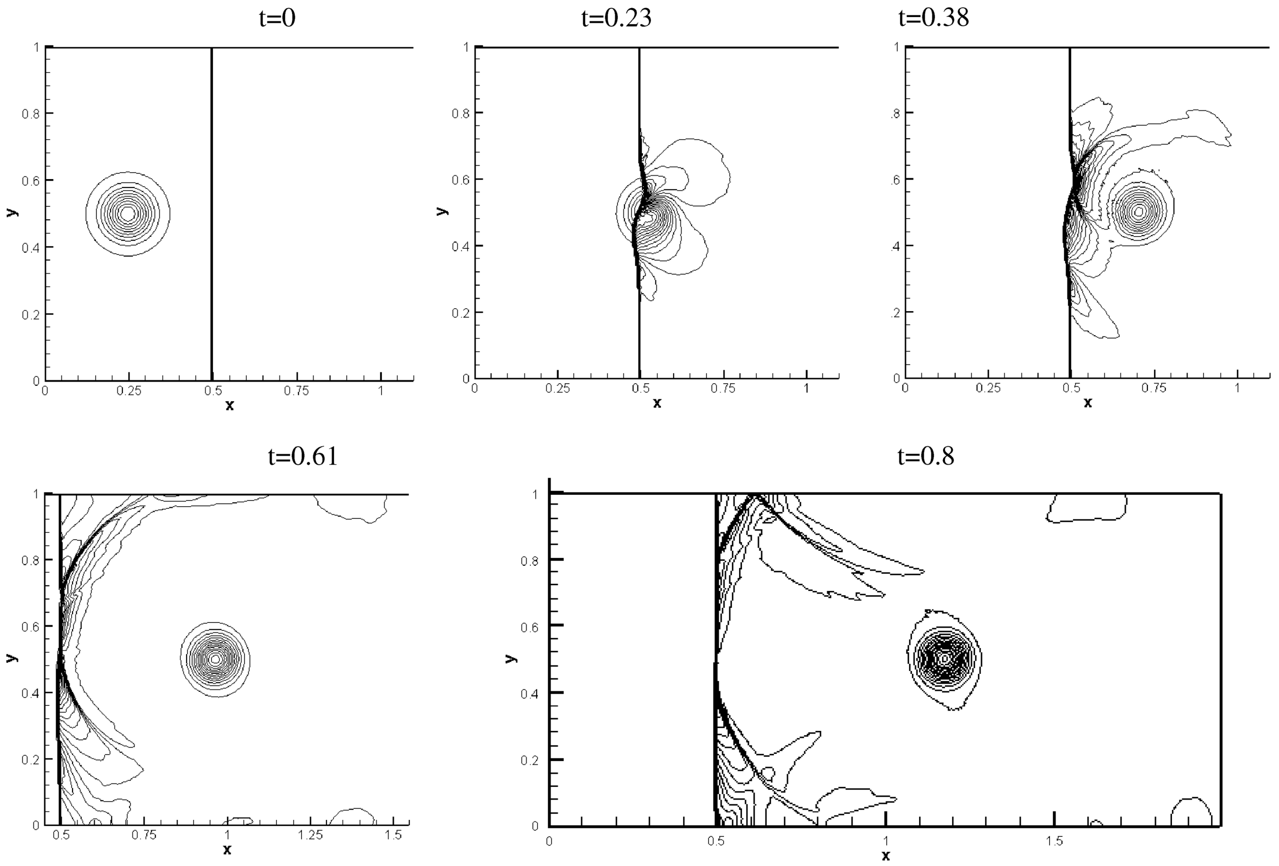
t=0 t=0.23 t=0.38

t=0.61 t=0.8

Fig. 7 Instantaneous density fields for the 2-D shock/weak-vortex interaction problem; 50 density contours are shown.

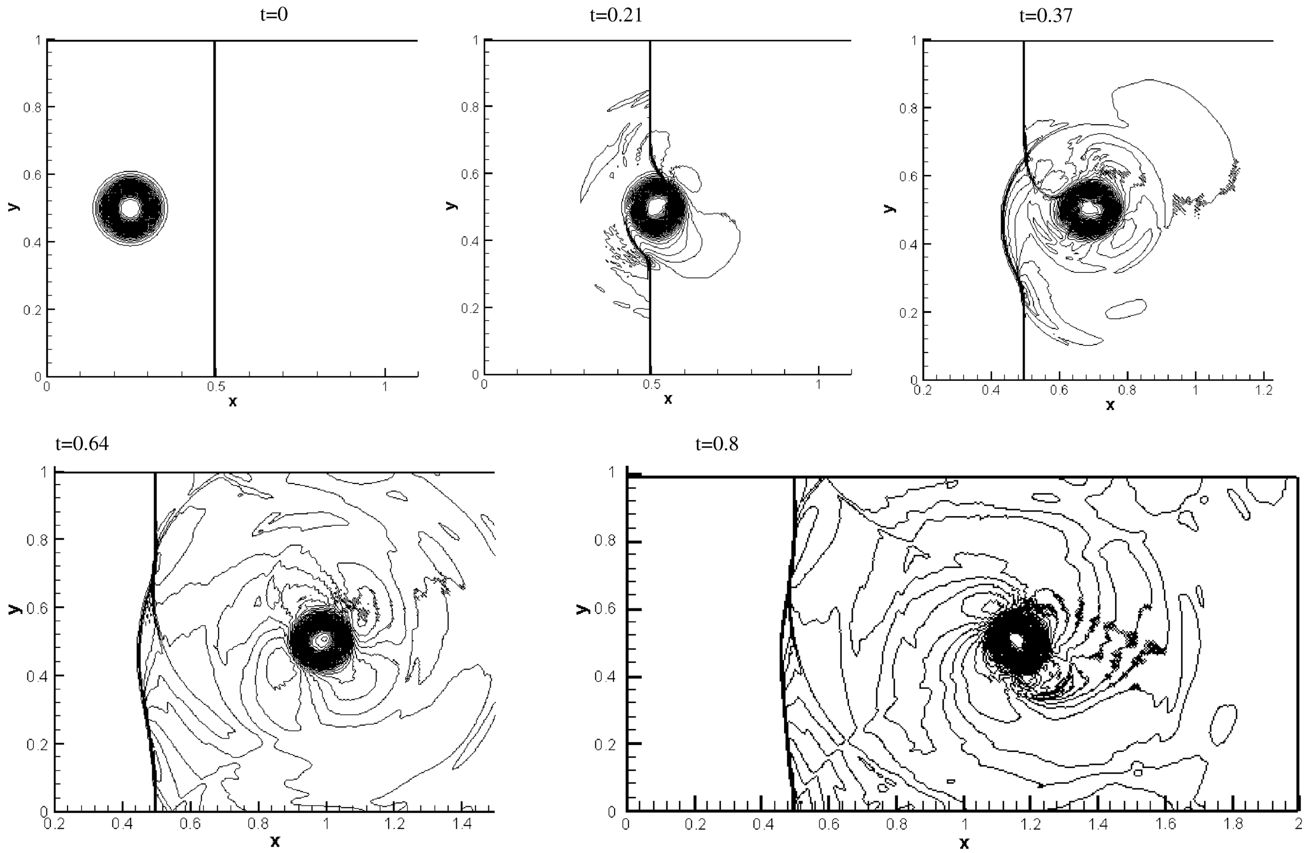
t=0 t=0.21 t=0.37

t=0.64 t=0.8

Fig. 8 Instantaneous density fields for the 2-D shock/strong-vortex interaction problem; 50 density contours are shown.

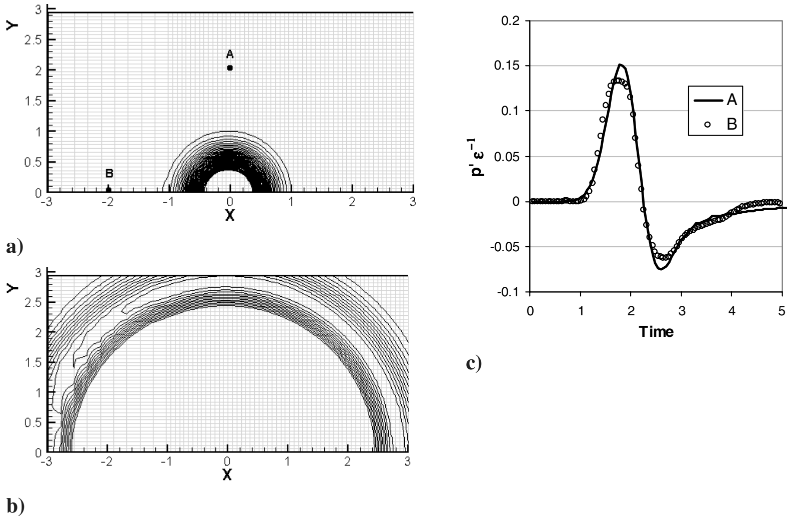

a)

b)

c)

Fig. 9 Computed pressure perturbation fields at two time moments, $t = 0 - (a)$ and $t = 2.4 - (b)$, for the 2-D problem of an acoustic Gaussian pulse evolving in open-domain free space field (50 contour lines of positive pressure perturbations are shown), and pressure–time signals obtained in points A and B (shown in Fig. 9a), which correspond to a fine and a coarse part of the grid.

50 cells, respectively. Across $x = -1$, the grid cell-size distribution thus has a discontinuity.

Instantaneous pressure perturbations normalized by the amplitude of the initial pulse,

$$p'\varepsilon^{-1} = \varepsilon^{-1}(p - p_\infty)/p_\infty$$

are shown in Figs. 9a and 9b. In the snapshots, a Gaussian-type pulse in pressure, which corresponds to the original pressure fluctuation, is shown to propagate through the computational domain without a noticeable attenuation of amplitude or loss of the solution symmetry due to spurious grid reflections during the pulse propagation through the fine/coarse-grid interface on the left. We emphasize that there was no special treatment of this grid singularity introduced in the CABARET scheme; the fact that the scheme is not sensitive to the grid nonsmoothness effects follows from its extremely compact computational stencil.

Figure 9c shows pressure–time signals obtained for two control points, A and B, which are positioned at the same distance $R = 2$ from the pulse center at 90 and 180 deg to the x axis. It was confirmed by a further grid refinement study that the solution obtained at point A is converged within less than 1% error in amplitude of the pressure peak and, therefore, will be further used as a reference solution. In the coarse region of the grid, at point B, the acoustic wave amplitude is reasonably well preserved (within 10–12%) and, again, shows no sign of spurious grid reflections.

V. Conclusions

A new efficient numerical method for linear and nonlinear acoustic problems is proposed. The method combines the simplicity of finite volume approaches, the physical insight of methods of characteristics, and low dispersive and dissipative behaviors of finite difference schemes.

Numerical results provided on uniform Cartesian grids demonstrate that the method is efficient in a range of linear and nonlinear inviscid problems. The extension of the method to more complicated grid geometries and viscous flows will be the subject of future publications.

Appendix: Matrices in Cartesian Coordinates

The matrices of primary variables and characteristic variables in 2-D Cartesian coordinates are given by

$$\mathbf{A} = \begin{pmatrix} u & \rho & 0 & 0 \\ 0 & u & 0 & 1/\rho \\ 0 & 0 & u & 0 \\ 0 & \rho\cdot c^2 & 0 & u \end{pmatrix}$$

$$\mathbf{B} = \begin{pmatrix} v & \rho & 0 & 0 \\ 0 & v & 0 & 1/\rho \\ 0 & 0 & v & 0 \\ 0 & \rho\cdot c^2 & 0 & u \end{pmatrix}$$

$$\mathbf{L}_x = \begin{pmatrix} 0 & 1 & 0 & 1/(\rho\cdot c) \\ 0 & 1 & 0 & -1/(\rho\cdot c) \\ 0 & 0 & 1 & 0 \\ -c^2 & 0 & 0 & 1 \end{pmatrix}$$

$$\mathbf{L}_y = \begin{pmatrix} 0 & 1 & 0 & 1/(\rho\cdot c) \\ 0 & 0 & 1 & 0 \\ 0 & 1 & 0 & -1/(\rho\cdot c) \\ -c^2 & 0 & 0 & 1 \end{pmatrix}$$

$$\Lambda_{\mathbf{x}} = \begin{pmatrix} u+c & & & \\ & u-c & & \\ & & u & \\ & & & u \end{pmatrix}$$

$$\Lambda_{\mathbf{y}} = \begin{pmatrix} v+c & & & \\ & v-c & & \\ & & v & \\ & & & v \end{pmatrix}$$

where c is the sound speed.

Acknowledgments

The support by the Royal Society of London is gratefully acknowledged. Work was also supported by the Russian Foundation for Basic Research.

References

[1] Colonius, T., and Lele, S. K., "Computational Aeroacoustics: Progress on Nonlinear Problems of Sound Generation," *Progress in Aerospace Sciences*, Vol. 40, No. 6, Aug. 2004, pp. 345–416. doi:10.1016/j.paerosci.2004.09.001

[2] Tam, C. K. W., and Webb. J. C., "Dispersion-Relation-Preserving Finite Difference Schemes for Computational Acoustics," *Journal of Computational Physics*, Vol. 107, No. 2, Aug. 1993, pp. 262–281. doi:10.1006/jcph.1993.1142

[3] Bogey, C., and Bailly, C., "A Family of Low Dispersive and Low Dissipative Explicit Schemes for Flow and Noise Computations," *Journal of Computational Physics*, Vol. 194, No. 1, Feb. 2004, pp. 194–214.
doi:10.1016/j.jcp.2003.09.003

[4] Shu, C. W., and Osher, S., "Efficient Implementation of Essentially Nonoscillatory Shock-Capturing Schemes," *Journal of Computational Physics*, Vol. 77, No. 2, Aug. 1988, pp. 439–471.
doi:10.1016/0021-9991(88)90177-5

[5] Liu, X. D., Osher, S., and Chan, T., "Weighted Essentially Nonoscillatory Schemes," *Journal of Computational Physics*, Vol. 115, No. 1, 1994, pp. 200–212.
doi:10.1006/jcph.1994.1187

[6] Titarev, V. A., and Toro, E. F., "ADER: Arbitrary High Order Godunov Approach," *Journal of Scientific Computing*, Vol. 17, Nos. 1–4, 2002, pp. 609–618.
doi:10.1023/A:1015126814947

[7] Atkins, H. L., and Shu, C. W., "Quadrature-Free Implementation of the Discontinuous Galerkin Method for Hyperbolic Equations," AIAA Paper 96-1683, 1996.

[8] Qiu, J., and Shu, C. W., "Runge–Kutta Discontinuous Galerkin Method Using WENO Limiters," *SIAM Journal on Scientific Computing*, Vol. 26, No. 3, 2005, 907–929.

[9] Wang, Z. J., "High-Order Spectral Volume Method for Benchmark Aeroacoustic Problems," 41st Aerospace Sciences Meeting and Exhibit, AIAA Paper 2003-0880, 2003.

[10] Harten, A., Engqist, B., Osher, S., and Chakravarthy, S., "Uniformly High Order Accurate Essentially Non-Oscillatory Schemes 3," *Journal of Computational Physics*, Vol. 71, No. 2, Aug. 1987, pp. 231–303.
doi:10.1016/0021-9991(87)90031-3

[11] Iserles, A., "Generalized Leapfrog Methods," *IMA Journal of Numerical Analysis*, Vol. 6, No. 4, 1986, pp. 381–392.
doi:10.1093/imanum/6.4.381

[12] Thomas, J. P., and Roe, P. L., "Development of Non-Dissipative Numerical Schemes for Computational Aeroacoustics," AIAA Paper 93-3382, 1993.

[13] Goloviznin, V. M., and Samarskii, A. A., "Difference Approximation of Convective Transport with Spatial Splitting of Time Derivative," *Mathematical Modelling*, Vol. 10, No. 1, 1998, pp. 86–100.

[14] Boris, J. P., Book, D. L., and Hain, K., "Flux-Corrected Transport 2: Generalization of the Method," *Journal of Computational Physics*, Vol. 18, July 1975, pp. 248–283.
doi:10.1016/0021-9991(75)90002-9

[15] Goloviznin, V. M., and Karabasov, S. A., "Non-Linear Correction of Cabaret Scheme," *Mathematical Modelling*, Vol. 10, No. 12, 1998, pp. 107–123.

[16] Goloviznin, V. M., "Balanced Characteristic Method for Systems of Hyperbolic Conservation Laws, *Doklady. Mathematics*, Vol. 72, No. 1, July–Aug. 2005, pp. 619–623.

[17] Hirsh, C., "*Numerical Computation of Internal and External Flows*, Vol. 2, Wiley, New York, 1998.

[18] Zhou, Y. C., and Wei, G. W., "High-Resolution Conjugate Filters for the Simulation of Flows," *Journal of Computational Physics*, Vol. 189, No. 1, 2003, pp. 159–179.
doi:10.1016/S0021-9991(03)00206-7

[19] Woodward, P., and Colella, P., "The Numerical Simulation of Two-Dimensional Fluid Flow with Strong Shocks," *Journal of Computational Physics*, Vol. 54, No. 1, 1984, pp. 115–173.
doi:10.1016/0021-9991(84)90142-6

[20] Lui, C., and Lele, S. K., "Direct Numerical Simulation of Spatially Developing, Compressible, Turbulent Mixing Layers," AIAA Paper 2001-0291, 2001.

K. Powell
Associate Editor